EPSC2018

LSE1/TP15 abstracts

13 Sep 2018 15:36:23

EPSC Abstracts
Vol. 12, EPSC2018-121-2, 2018
European Planetary Science Congress 2018

Application of Machine Learning to Giant Impact Studies

Saverio Cambioni[1], Travis S.J. Gabriel[2], Erik Asphaug[1], Roberto Furfaro[3], Alexandre Emsenhuber[1] and Stephen Schwartz[1]
[1]Lunar and Planetary Laboratory, The University of Arizona, Tucson AZ, USA (cambioni@lpl.arizona.edu)
[2]School of Earth and Space Exploration, Arizona State University, Tempe, AZ, USA,
[3]System and Industrial Engineering, The University of Arizona, Tucson, AZ, USA

Abstract

Giant impacts heavily influenced the final configuration and geochemistry of the terrestrial planets. In this study we use machine learning to explore a rich dataset of giant impact simulations in a supervised fashion. This new methodology produces mappings of giant impact outcomes in an *N*-Dimensional (*N*-D) parameter space, e.g., mass of target, target-projectile mass ratio, impact velocity and impact angle. We discuss the physical insights emerging from this initial analysis and future work.

1. Introduction

Bombardment by large projectiles played a key role in the formation of the inner planets through accumulation of rocky planetesimals. Our group uses Smoothed-Particle Hydrodynamics (SPH) to model giant impacts on planetary bodies such as the Moon, Mercury and Mars (e.g. [3,5,6]). As of today, our dataset is composed of over 1,500 simulations spanning a wide range of parameters (composition, size, mass ratio, impact angle, impact velocity). Each SPH outcome is a complex *N*-D state (consolidated planets, clumps, unconsolidated ejecta, and their characteristics including thermodynamic states, etc.) that requires detailed analysis.

In this regard, state-of-the-art machine learning techniques allow for several advantages: 1) they can streamline the generation of data sets to most efficiently explore regions of interest in a large parameter space; and 2) they can perform accurate mappings of initial conditions and end-states, with associated probabilities, taking into account a high-dimensional parameter space. This is in contrast to human operators that are often limited to a mostly 2-D understanding of the data. Modern machine learning schemes take advantage of this big data problem to spot new and sometimes unexpected correlations.

In this pilot study, we trained, tested and validated an algorithm able to map strictly the pre-impact conditions to the accretion efficiency (defined as the fraction of the projectile mass $M_{p.}$ acquired by the target M_t). The adopted scheme is supervised: the machine learns the correlation between input and output using labelled data: $\{\mathbf{x_i}; y_i\}$, where $\mathbf{x_i}$ is an array of four input parameters (predictors): M_t (mass of the target), $M_{p.}$ (mass of the impactor), θ (impact angle) and the ratio between the impact velocity and the escape velocity; and y_i is the corresponding response. Efficiency, accuracy, and predictive power will be discussed.

2. Classification model

In SPH, the continuous fluid is represented as a Lagrangian set of particles that move with the flow; this allows easy visualization and supports analytical deductions ([4] and references therein). We designed a naive Bayesian classifier [7] based on a visual classification of simulation outcomes. Fig. 1 shows an example of *a posteriori* classification probability for 4 distinct impact outcomes defined and discussed in [1,4,8]: Hit & Run, Graze & Merge, Merge, Disruption. Each of these collisional regimes can be thought of as a 'phase' in which collisional behaviour is similar, that is, a scaling law can be expected to apply. The topology reveals relatively narrow transition regions between the different collisional regimes, in which the collisional outcome associated with a combination of parameters is probabilistic. The classifier can be adopted as a guideline to distinguish "interesting" regions of phase-space to be followed up with further simulations.

3. Surrogate model

While a classifier is able to handle discrete, qualitative responses, a surrogate model is an algorithm able to mimic the SPH physics and to predict continuous (floating point) outputs given the input parameters (predictors). Running the surrogate model drastically reduces the computational time with respect to full

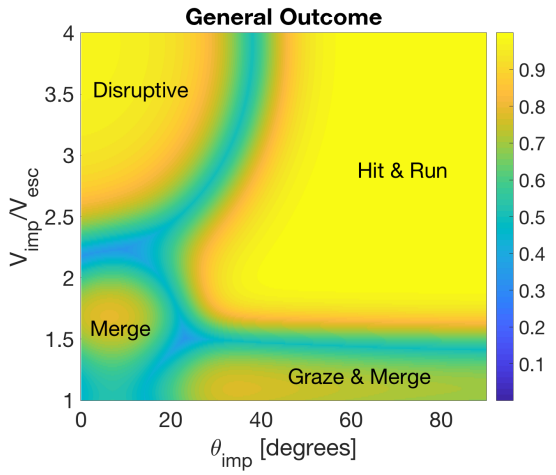

Figure 2. Example of a posteriori probability distribution for the 4 outcome categories ($M_t = 0.1M_{Earth}$ and $\gamma = M_p/M_t = 0.7$).

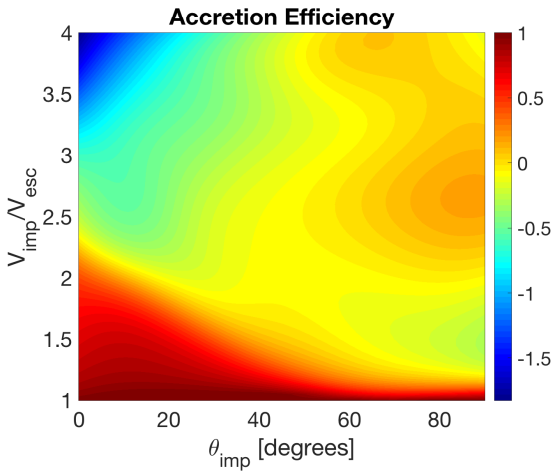

Figure 2. Example of prediction for accretion efficiency using the designed surrogate model ($Mt = 0.1M_{Earth}$ and $\gamma = M_p/M_t = 0.7$).

SPH simulations (from hours to seconds). The surrogate model forecasts accretion efficiency at several times the gravitational timescale, after pressure gradient forces are no longer acting. The accretion efficiency map, Fig. 2, is richer in terms of collisional outcomes with respect to the Bayesian classifier. We note that a significant fraction of the projectile mass M_p can be acquired by the target M_t in 'Hit & Run' collisions too, without a complete merging of the projectile with the target. Conversely, 'Graze & Merge' collisions at low velocity and high impact angle can somewhat be inefficient, implying that a significant fraction of mass ends up forming unbounded remnants.

4. Conclusions and future work

This study shows the potentialities of machine learning in: 1) processing large planetary formation datasets without a heavy involvement/bias from the user; 2) identifying "strange" or interesting regions in the parameter space requiring further study; 3) providing a statistical description to phase boundaries as opposed to the hardline boundaries of traditional scaling laws. One long-term scientific goal is to obtain systematic guidance to solutions of complex problems such as Earth-Moon system formation and Mercury formation [6, 3] that may exist on phase boundaries in outcomes of giant impacts.

In future work we will create a complete surrogate SPH model that can enable additional outputs such as masses, velocities and spin states of the largest remnants. We will also apply this approach to the transition from gravity- to friction-dominated collisions. The surrogate model could be subsequently used as input in *N*-body simulations for post-collisional dynamical studies. Being an invertible function, we can apply the surrogate model to gain a better understanding of the relative likelihoods of any specific giant impact scenario.

References

[1] Asphaug, E., et al.: Hit-and-run planetary collisions, Nature, Vol. 439.7073, pp. 155, 2006.

[2] Asphaug, E.: Impact origin of the Moon? Annual Review of Earth and Planetary Sciences, Vol. 42, pp. 551-578, 2014.

[3] Asphaug, E., and Reufer, A.: Mercury and other iron-rich planetary bodies as relics of inefficient accretion, Nature Geoscience, Vol. 7.8, pp. 564, 2014.

[4] Asphaug, E., et al.: Global scale impacts, Asteroid IV, University of Arizona Press, 2015.

[5] Emsenhuber, A., et al.: SPH calculations of Mars-scale collisions: The role of the equation of state, material rheologies, and numerical effects, Icarus, Vol. 301, pp. 247-257, 2018.

[6] Reufer, Andreas, et al.: A hit-and-run giant impact scenario, Icarus, Vol. 221.1, pp. 296-299, 2012.

[7] Rish, I.: An empirical study of the naive Bayes classifier, IJCAI 2001 workshop, IBM, Vol. 3, n. 22, pp. 41-46, 2001.

[8] Stewart, T., and Leinhardt, Z.: Velocity-dependent catastrophic disruption criteria for planetesimals, The Astrophysical Journal Letters, Vol. 691.2, pp. L133, 2009.

EPSC Abstracts
Vol. 12, EPSC2018-196-1, 2018
European Planetary Science Congress 2018

Sequential Giant Impacts

Alexandre Emsenhuber and Erik Asphaug
University of Arizona, Lunar and Planetary Laboratory, Tucson, Arizona, United States (emsenhuber@lpl.arizona.edu)

Abstract

Collisions between similar sized bodies often result in multiple remnants. We study two most common pathways of growth during 'late stage' accretion, which are graze and merge, and hit and run return where a hit and run is followed by a slower accretionary encounter, accounting for the presence of the Sun or a central planet. With initial N-body study we find that in case of an hit and run return the impact velocity is mostly determined for the prior impact while impact angle and direction are not. This has implications for the formation of our Moon if resulted from a hit and run collision, as the disk would be offset relative to the equator of the Earth.

1. Introduction

Collisions at near-escaping velocities between similar-sized planetary bodies (i.e. giant impacts) are seldom efficient when it comes to accretion. More often than not, a significant part of the smaller, the impactor, 'misses' the target, leading to the collision resulting in multiple remnants [1]. This part of the impactor becomes either a 'runner' stripped of its exterior materials, or fragments into a suite of genetically-correlated smaller planets. The relative velocity is decreased following the collision; when the bodies remain gravitationally bound, the result is successive collisions separated a day or so in the case of graze and merge collisions (GMC) [6]. When not, the result is hit and run collision (HRC) where the runner eventually returns in a time scale of thousands to millions of years [4], leading to a hit and run return collision (HRR).

2. Methods

Collisions are modelled with the SPH technique using a code suited for large scale collisions and that includes a strength model for solid friction [7, 3]. We model both kinds of accretions, and study the thermodynamic (P, T) evolution and spatial mixing of particles to ascertain the effectiveness of successive giant impacts, especially on isotopic equilibration and formation of large satellites. GMC can be studied using uninterrupted hydrocode simulations, provided the dynamics of the runner is advanced accurately enough to predict the angle and velocity of the return collision, upon which the final outcome depends sensitively. When graze and merge happens in orbit around a planet or close to a star, however, GMC can becomes HRC if the bodies range beyond the Hill sphere. In the case of HRC the escaping runner must be tracked for many orbits until its next encounter with the target; this can be a close encounter leading to escape of the runner, or a follow-on collision that we model by mapping the outcome of one hydrodynamical simulation into another. We map the target and runner emerging from one collision (ignoring lost collision products) into an N-body code, assuming a range of possible pre-impact orbits following [5]. This provides timing, velocity and geometry constraints for the return collision.

3. Results

In our initial N-body studies we find that the impact velocity of the return collision is mostly determined from the end conditions of the prior collision, with a greater dispersion in impact velocity as the time between collisions increases (Fig. 1). The presence of other planets in the system causes a further increase in the dispersion of impact velocities, but barely affects the delay between the collisions. On the other hand, the impact direction and angle are essentially unconstrained.

4. Discussion and outlook

Hit and run return and graze and merge are the most common mechanisms of late stage accretion; in either case the second impact must be modeled with some precision to understand the actual outcome. This results in sensitivity of the outcome to parameters such as impact velocity, impact angle and rotation state and composition, and also orbital dynamics of the collid-

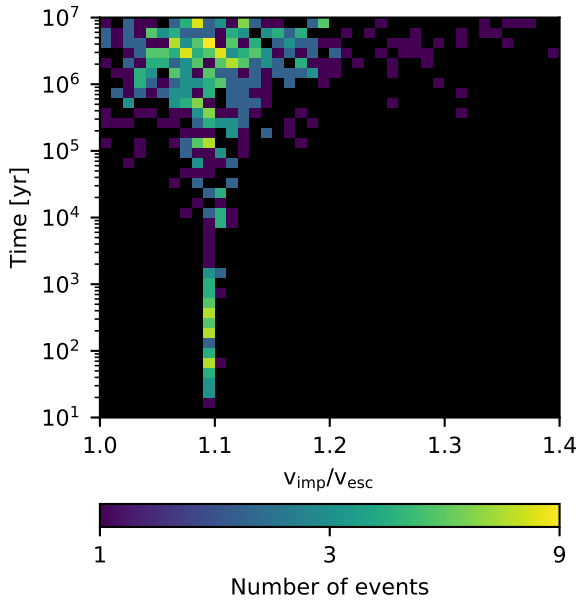

Figure 1: Correlation between the impact velocity versus delay between the successive collision for an hit and run return case. The characteristics of the prior collision are $m_{\rm tar} = 1$ M$_\oplus$, $m_{\rm imp}/m_{\rm tar} = 0.1$, $v_{\rm imp}/v_{\rm esc} = 1.2$ and $\theta = 50^\circ$. It results in two remnants with a mass ratio $m_{\rm slr}/m_{\rm lr} = 0.078$ and a relative velocity such that the return collision would have $v_{\rm imp}/v_{\rm esc} = 1.099$ if the value was conserved.

ing bodies around the Sun, or around a central planet. Runners emerge at a reduced relative velocity, and are smaller than the projectiles that made them. The follow-on giant impact in HRR is therefore expected to strongly favor merger compared to the first giant impact. This means that a first return is more common than a subsequent return and so on. However, a simple merger is rare, that is not a graze and merge [2]. Lastly, since the specific geometry (though not the velocity) of the second encounter is random, we consider how HRR might establish an offset between the spin axis of the merged body and the disk material that is launched in the original collision. If Theia and proto-Earth accreted by HRR, then the protolunar disk spawned by the first collision would be offset relative to the equator of the Earth. We use this dynamical constraint to begin to identify scenarios for Moon formation as a sequential merger.

References

[1] Asphaug E., Agnor, C. B. and Williams, Q.: Hit-and-run planetary collisions, Nature, Vol. 439, pp. 155-160, 2006.

[2] Cambioni, S., Gabriel, T. S. J., Asphaug, E., Furfaro, R., Emsenhuber, A. and Schwartz, S.: Application of Machine Learning to Giant Impact Studies, EPSC Abstracts, Vol. 12, 2018.

[3] Emsenhuber, A., Jutzi M. and Benz W.: SPH calculations of Mars-scale collisions: The role of the equation of state, material rheologies, and numerical effects, Icarus, Vol. 301, pp. 247-257, 2018.

[4] Jackson, A. P. and Wyatt, M. C.: Debris from terrestrial planet formation: the Moon-forming collision, MNRAS, Vol. 425 pp. 657-679, 2012.

[5] Jackson, A. P., Gabriel, T. S. J. and Asphaug, E. I.: Constraints on the pre-impact orbits of Solar sysren giant impactors, MNRAS, Vol. 474, pp. 2924-2936, 2018.

[6] Leinhardt, Z. M., Marcus, R. A. and Stewart, S. T.: The Formation of the Collisional Family Around the Dwarf Planet Haumea, ApJ, Vol. 714, pp. 1789-1799, 2010.

[7] Reufer, A., Meier, M. M. M., Benz, W. and Wieler, R.: A hit-and-run giant impact scenario, Icarus, Vol. 221, pp. 296-299, 2012.

EPSC Abstracts
Vol. 12, EPSC2018-291, 2018
European Planetary Science Congress 2018

Early evolution of Venus and Earth constrained by the reproduction of measured Ar, Ne isotope and K/U elemental ratios

Helmut Lammer, (1), Martin Leitzinger (2,1), Petra Odert (1), Christoph Burger (3), Darya Kubyshkina (1), Manuel Scherf (1), Thomas Maindl (3), Colin Johnstone (3), Nicola Tosi (4,5), Athanasia Nikolaou (4,5), Emmanuel Marcq (6), Luca Fossati (1), Nikolai V. Erkaev (7, 8), Manuel Güdel (3), Lena Noak (9), Kristina G. Kislyakova (3,1), Florian Ragossnig (3), Elke Pilat-Lohinger (3)

(1) Space Research Institute, Austrian Academy of Sciences, Graz, Austria, (2) Institute of Physics/IGAM, University of Graz, Austria, (3) Department of Astrophysics, University of Vienna, Austria, (4) Institute of Planetary Research, Department of Planetary Physics, DLR, Berlin Germany, (5) Department of Astronomy and Astrophysics, Berlin Institute of Technology, Germany, (6) LATMOS, Université de Versailles Saint-Quentin-en-Yvelines, Guyancourt, France, (7) Institute of Computational Modelling, FRC Krasnoyarsk Science Center SB RAS, Krasnoyarsk, Russian Federation, (8) Siberian Federal University, Krasnoyarsk, Russian Federation, (9) Department of Earth Sciences, Freie Universität Berlin, Germany

Abstract

We show that the measured present day atmospheric Ar, Ne isotope ratios and elemental K/U ratios measured for Venus and Earth can be reproduced by a combination of EUV-driven hydrodynamic hydrogen escape and impacts happening during accretion. We find that both protoplanets formed within the solar nebula and accreted large enough masses able to capture thin hydrogen envelopes, which were then lost within a few 10s of million years after disk dispersal. We further show that early Venus was surrounded by a denser primordial hydrogen-dominated atmosphere compared to a less massive proto-Earth that accreted its final mass by pre-fractionated dry impactors and about two percent carbonaceous chondrites after the thin primordial hydrogen envelope was lost. Our results agree with hafnium-wolfram isotope chronometric evidence that favors a fast accretion scenario of the Earth with a late Moon-forming impact. We conclude with a discussion on the implications of these findings in relation to planetary evolution of terrestrial exoplanets and their potential habitability.

Acknowledgements

We acknowledge support by theAustrian Fonds zur Förderung der Wissenschaftlichen Forschung, Nationales Forschungs Netzwerk (FWF NFN) project S116-N16 and the subprojects S11603-N16, S11604-N16, S11606-N16, and S11607-N16. H.L, M.L. and P.O. acknowledge support of the FWF project P27256-N27. D.K. and L.F. acknowledge the Austrian Forschungsförderungsgesellschaft FFG project “TAPAS4CHEOPS” P853993. The authors thank ISSI for the support of the ISSI team ”The early evolution of the atmospheres of Earth, Venus, and Mars”. N.T. and A.N. acknowledge support from the Helmholtz Association (project VH-NG-1017). M. Güdel and L. Noack acknowledge the collaboration within the COST Action TD 1308. The authors also thank the International Space Science Institute (ISSI) in Bern, the ISSI-Beijing team “Astrobiology” and the ISSI team“The Early Evolution of the Atmospheres of Earth, Venus, and Mars”.

EPSC Abstracts
Vol. 12, EPSC2018-305, 2018
European Planetary Science Congress 2018

Escape and fractionation of elements from planetary embryos

Markus Benedikt (1), Manuel Scherf (1), Helmut Lammer (1), Emmanuel Marcq (2), Petra Odert (1), Martin Leitzinger (3)

(1) Space Research Institute, Austrian Academy of Sciences, Graz, Austria, (2) LATMOS, Université de Versailles Saint-Quentin-en-Yvelines, Guyancourt, France, (3) Institute of Physics/IGAM, University of Graz, Austria

Abstract

In the early evolution of planetary systems, protoplanets originate from the coagulation of dust and ice and initially reside embedded in the gas of the circumstellar disks. From isotope studies, it is expected that the Earth (and terrestrial planets) formed from pre-fractionated differentiated planetary embryos and a few percent carbonaceous chondrites. Large planetesimals and planetary embryos are differentiated bodies with sizes of several hundred to a few thousand kilometers. Planetary embryos form protoplanets via mutual collisions, which can lead to the development of magma oceans. During their solidification, significant amounts of the mantles' volatile contents may be outgassed. We show that the resulting steam atmospheres can be lost efficiently via hydrodynamic escape that drag heavier elements like noble gases, K, Na, Mn, Mg, P, etc. into space so that they are also lost. Planetary embryos that are later involved in terrestrial planet formation can be drier than previously expected. We model the outgassing and subsequent hydrodynamic escape of steam atmospheres from such embryos, including the efficient outflow of H that drags along heavier species like O, CO2, CO, K, Na, Mn, Mg, P, etc., and noble gases (Ar, Ne, Xe, Kr) and their isotopes. The full range of possible EUV evolution tracks of a young solar-mass star is taken into account. We investigate the atmospheric/elemental escape from Moon, 0.5Mars-, Mars- and 1.5Mars-sized planetary embryos at different orbital distances. Finally, we discuss the implications of our findings in relation to elemental composition of the bulk silicate Earth composition.

Acknowledgements

We acknowledge support by the Austrian Fonds zur Förderung der Wissenschaftlichen Forschung, Nationales Forschungs Netzwerk (FWF NFN) project S116-N16 and the subprojects, S11606-N16, and S11607-N16. H.L, M.L. and P.O. acknowledge also support of the FWF project P27256-N27.

EPSC Abstracts
Vol. 12, EPSC2018-351, 2018
European Planetary Science Congress 2018

The Pb-Pb chronology of impact melt rock 14310 and new crater size-frequency distribution measurements of the Apollo 14 landing site

Danil Borisov (1), Harald Hiesinger (1), Thomas Haber (2), Erik Scherer (2), Wajiha Iqbal (1), and Carolyn van der Bogert (1)

(1) Institut für Planetologie, Westfälische Wilhelms-Universität Münster, Wilhelm-Klemm-Str. 10, D-48149 Münster, Germany (d.borisov@uni-muenster.de), (2) Institut für Mineralogie, Westfälische Wilhelms-Universität Münster, Corrensstr. 24, D-48149 Münster, Germany

1. Introduction

The dating of geological units and events on the Moon is achieved by two inherently different approaches: (1) radiogenic isotope dating of returned lunar samples or meteorites and (2) model age determination using crater size-frequency distributions (CSFDs). Combining the results from both approaches applied to Apollo and Luna landing sites has allowed the development of the lunar cratering chronology, which enables absolute model ages to be derived from CSFDs of unsampled regions on the Moon [e.g., 1]. Since the initial development of the lunar cratering chronology, both age determinations through radiogenic isotope ratios and CSFD dating techniques have advanced, and recent orbital missions have collected new global datasets, allowing us to re-evaluate and update the calibration points for the cratering chronology. Here, we combine both dating techniques to reinvestigate the Apollo 14 landing site.

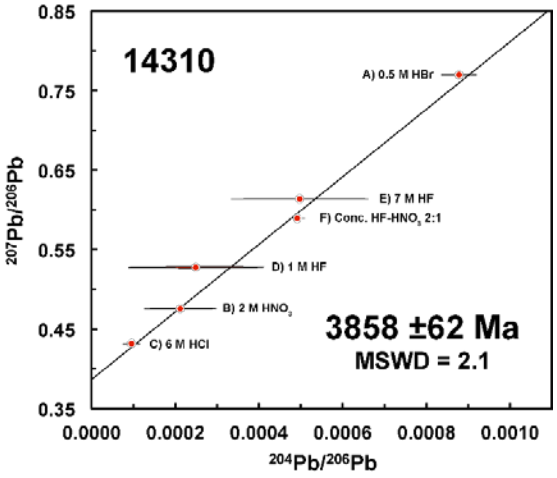

Figure 1: Inverse Pb-Pb isochron diagram for a bulk fine-grained fraction of sample 14310.

2. Pb-Pb Dating

The pioneering U-Th-Pb studies of sample 14310 performed in the early 1970s yielded dates of ca. 3.8-3.9 Ga [e.g., 2], which were interpreted to represent the crystallization age of this rock. We are carrying out Pb-Pb analyses to complement our multi-system (Sm-Nd, Lu-Hf, Rb-Sr) chronological work on this sample [3], with the aim of testing for concordance among isotope systems and precisely constraining the crystallization age. For our Pb-Pb work, each mineral concentrate was subjected to a 12-step washing and progressive digestion procedure in an attempt to better separate radiogenic, initial, and contaminating Pb components [e.g., 4, 5, 6]. The earlier U-Th-Pb studies [e.g., 2] did not do this, as it would have potentially fractionated these elements. Figure 1 shows our inverse Pb-Pb isochron obtained for a bulk fine-grained fraction (<65 µm) of 14310, which yields a date of 3858 ±62 Ma that is concordant with the Rb-Sr, Sm-Nd, and Lu-Hf dates that we have obtained on the same sample split.

3. Apollo 14 Landing Site

The Apollo 14 landing site is situated about 600-800 km south of the Imbrium basin within the Fra Mauro Formation (FMF), which has been interpreted to be Imbrium ejecta [e.g., 7]. The landing site was originally chosen to sample ejecta blocks that were excavated from the very young and nearby Cone crater, and interpreted to unambiguously represent the FMF [7]. Sampling the ca. 30 Ma Cone crater has also provided an important anchor point for young lunar surfaces [e.g., 8]. The presence of old and young surface units make the Apollo 14 landing site especially worthy of reinvestigation, as we can potentially constrain the lunar cratering chronology for both old and young ages.

4. CSFD Measurements

The originally reported $N(1)$ value of $3.7 \pm 0.7 \times 10^{-2}$ yielded an estimated age of the FMF of 3.91 ± 0.1 Ga [1]. We used the global Wide Angle Camera (WAC) mosaic (100 m/pixel; incidence angle: 60°) to perform new CSFD measurements on the same counting area and report a $N(1)$ value of 4.23×10^{-2}, which was fit with the lunar chronology function, yielding an age of 3.94 ± 0.02 Ga, as seen in Figure 2. This result is within the uncertainty of [1] and agrees with recent Imbrium age estimations of 3.91-3.94 Ga [e.g., 9].

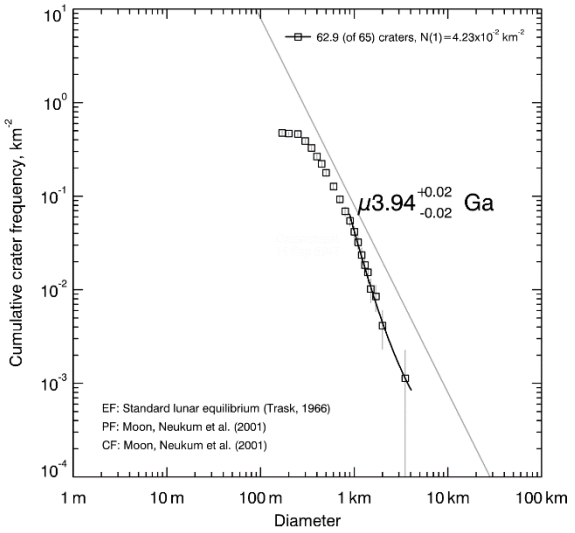

Figure 2: Re-counted cumulative CSFD for the original area selected by [1] for Apollo 14.

5. Outlook

Our preliminary results indicate that sample 14310 is younger than the Imbrium basin, if we assume the most recent age estimate of 3.91-3.94 Ga [e.g., 9], which we were able to reproduce with our CSFD measurements based on the global WAC mosaic. We are currently performing CSFD measurements based on Near Angle Camera (NAC) data to better constrain the $N(1)$ value of the FMF and will present the results at the meeting. Additionally, we will aim to identify potential source craters of 14310 and discuss possible implications on the lunar cratering chronology. Ultimately, this ongoing study aims to combine both laboratory and remote sensing investigations to reveal new constraints on the age of the Imbrium basin formation event.

References

[1] Neukum, G.: Habilitation thesis, University of Munich, 1983.

[2] Tatsumoto, M.: U-Th-Pb and Rb-Sr Measurements on Some Apollo 14 Lunar Samples, Lunar and Planetary Science Conference, 10-13 January 1972, Houston, USA, 1972.

[3] Haber, T.: ^{176}Lu-^{176}Hf Isochron Dating of Strongly Cosmic Ray Exposed Samples - A Case Study on Apollo 14 Impact Melt Rock 14310, Lunar and Planetary Science Conference, 20-24 March 2017, Houston, USA, 2017.

[4] Frei, R. and Kamber, B. S.: Single mineral Pb-Pb dating, Earth and Planetary Science Letters, Volume 129, pp. 261-268.

[5] Connelly, J. N., Bollard, J., and Bizzarro, M.: Pb-Pb chronometry and the early Solar System, Geochimica et Cosmochimica Acta, Volume 201, pp. 345-363, 2017.

[6] Borg, L. E., et al.: Chronological evidence that the Moon is either young or did not have a global magma ocean. Nature, Volume 477, pp. 70–72, 2011.

[7] Swann, G. A. et al.: Geology of the Apollo 14 landing site in the Fra Mauro highlands, United States Government Printing Office, Washington, 1977.

[8] Hiesinger, H., et al.: New Crater Size-Frequency Distribution Measurements for Cone Crater at the Apollo 14 Landing Site, Lunar and Planetary Science Conference, 16-20 March 2015, Houston, USA, 2015.

[9] Bottke, W. F. and Norman, M. D.: The Late Heavy Bombardment, Annual Review of Earth and Planetary Sciences, Volume 45, pp. 619-647, 2017.

EPSC Abstracts
Vol. 12, EPSC2018-360, 2018
European Planetary Science Congress 2018

The age of lunar impact melt rock 67935 – Imbrium or not?

Thomas Haber, Erik E. Scherer
Westfälische Wilhelms-Universität Münster, Institut für Mineralogie, Corrensstr. 24, D-48149 Münster, Germany
(thomas.haber@wwu.de)

1. Introduction

Apollo 16 sample 67935 belongs to the so-called "mafic melt breccias" presumably formed during the Imbrium event [1], which most likely happened 3910-3940 Ma [2]. However, an old ^{187}Re-^{187}Os date (4210 ±130 Ma [3]) for sample 67935 is inconsistent with an Imbrium origin. To resolve this contradiction, we are trying to date this sample using a multichronometer approach, in which ^{176}Lu-^{176}Hf, ^{147}Sm-^{143}Nd, ^{87}Rb-^{87}Sr, and Pb-Pb are analysed on the same split [4, 5].

2. Methods and Results

We were allocated a ~1 g aliquot (,39) of 67935 comprising 2 pieces. White clasts were present in both pieces, and glass veins intruded the larger piece. During crushing, the clasts and glass phases were separated. This sample is too fine-grained (~20 µm) for standard magnetic separation procedures. To solve this problem, we developed an enclosed system for magnetic separation in ethanol [6] (based on [7]). With this setup, we successfully separated six compositionally different mineral fractions from a ≤ 20-µm bulk fraction. The separates, numbered 1 to 6 grade continuously from dark grey and most magnetic (#1) to light grey and least magnetic (#6). After digestion, elements for all six separates plus a 'bulk fine' fraction (whole rock fraction from which metal was removed using a hand magnet) were separated following the two-stage elution scheme of [8], followed by additional steps to separate Sm and Nd (using Ln-Spec columns), and to clean up the Sr fraction (using Sr-Spec columns). Strontium was measured on a Thermo Triton MC-TIMS, and all other elements (Lu, Hf, Rb, Sm, and Nd) on a Neptune Plus MC-ICP-MS.

The resulting ranges in parent-daughter ratios are ^{176}Lu/^{177}Hf: 0.017-0.022, ^{147}Sm/^{144}Nd: 0.161-0.174, and ^{87}Rb/^{86}Sr: 0.024-0.081 and all three systems have apparently been disturbed. Using all 7 isochron points does not yield a statistically relevant isochron for any of the three systems (Lu-Hf: 2689 ±1400 Ma, MSWD = 181; Rb-Sr: 4527 ±550 Ma, MSWD = 20; Sm-Nd: 3614 ±560 Ma, MSWD = 9.5). When excluding #3 and #4, the remaining 4 mineral fractions and the 'bulk fine' fraction yield a 3902 ±160 Ma Sm-Nd isochron (MSWD = 1.4, Figure 1C). The Lu-Hf and Sm-Nd isotopic systematics of samples on the lunar surface can be affected by neutron capture (NC) effects [9], which then would have to be corrected [4, 10]. However, no resolvable ^{180}Hf/^{177}Hf or ^{149}Sm/^{152}Sm anomalies were found when measuring an unspiked 'bulk fine' fraction. This indicates that no significant NC effects are present, and thus no correction was applied.

3. Discussion and Future Work

As can be seen in Figure 1A and 1B, the scatter in the Rb-Sr and Lu-Hf systems significantly exceeds the area covered by the two reference isochrons that reflect the two most likely ages of this sample. Thus, those two systems cannot be used to better constrain the age of sample 67935. However, our 5 of 7 point ^{147}Sm-^{143}Nd isochron date (3902 ±160 Ma, Figure 1C) is distinct from the 4210 ±130 Ma ^{187}Re-^{187}Os date of [3], but is in line with a 3910-3940 Ma Imbrium age [2]. At the moment however, we do not understand why points #3 and #4 deviate from the isochron.

We will analyse all six mineral separates with Raman spectroscopy to identify the minerals present and to better discern the differences between them. Furthermore, we are in the process of analysing the glass and clast fractions, which were separated from the sample during sample preparation. Some of our analysed mineral fractions might be "contaminated" with clast or glassy material. Thus, identifying the isotopic compositions of these two components could help to quantify the contamination and explain at least some of the scatter in our isochron plots. We will also try to date the sample using Pb-Pb as we recently did for 14310 [5].

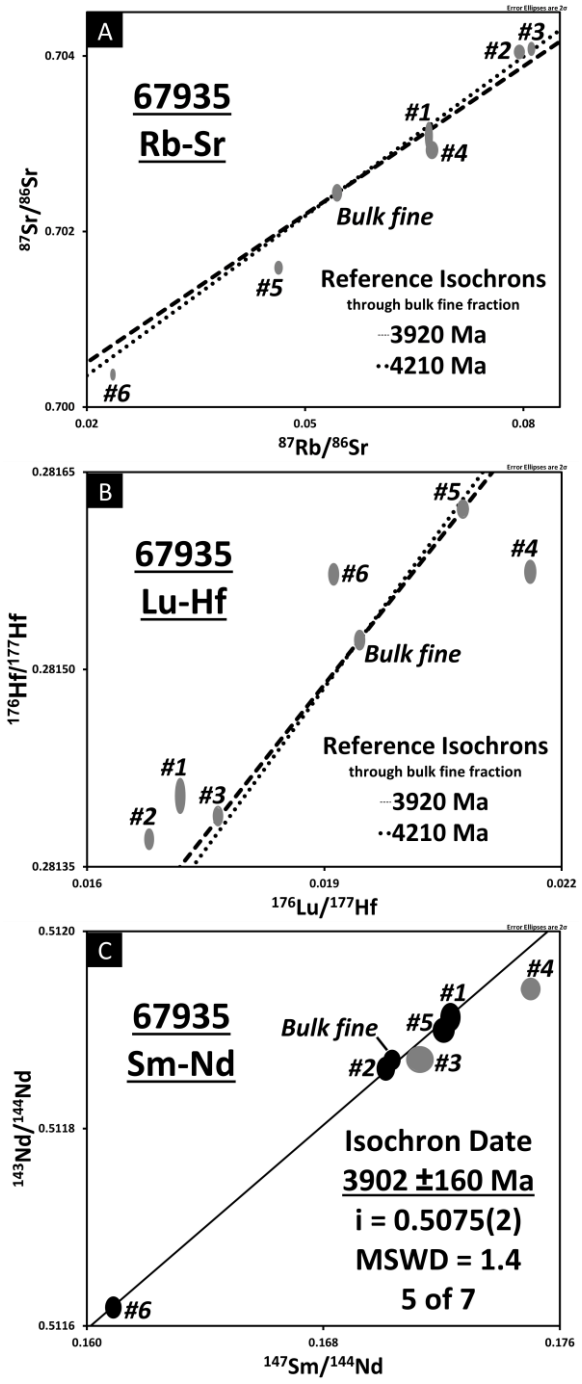

Figure 1: ^{87}Rb-^{87}Sr (A), ^{176}Lu-^{176}Hf (B), and ^{147}Sm-^{143}Nd (C) data obtained here for 67935. Reference isochrons are shown in panels A and B. The ^{147}Sm-^{143}Nd isochron (3902 ±160 Ma) through the bulk fine and 4 mineral fractions (#1, #2, #5, and #6) is shown in panel C. Error ellipses are 2σ standard deviation.

References

[1] Haskin, L. A., Korotev, R. L., Rockow, K. M., and Jolliff, B. L.: The case for an Imbrium origin of the Apollo thorium-rich impact-melt breccias, MAPS, 33, pp. 959–975, 1998.

[2] Bottke, W. F. and Norman, M. D.: The Late Heavy Bombardment, Annu. Rev. Earth Planet. Sci., 45, pp. 619–647, 2017.

[3] Fischer-Gödde, M. and Becker, H.: Osmium isotope and highly siderophile element constraints on ages and nature of meteoritic components in ancient lunar impact rocks, GCA, 77, pp. 135–156, 2012.

[4] Haber, T., Scherer, E. E., Bast, R., and Sprung, P.: ^{176}Lu-^{176}Hf Isochron Dating of Strongly Cosmic Ray Exposed Samples – A case study on Apollo 14 Impact Melt Rock 14310, LPSC XLVIII, Abstract 2911, 2017.

[5] Borisov, D., Hiesinger, H., Scherer, E. E., Haber, T., Iqbal, W., and van der Bogert, C. H.: An interdisciplinary re-investigation of the Apollo 14 landing site – Pb-Pb chronology of the impact melt rock 14310 and new crater size-frequency distribution measurements, LPSC XLIX, Abstract 1933, 2018.

[6] Haber, T. and Scherer, E. E.: Separating ≤ 20 µm sized mineral fractions for geochronology of lunar sample 67935, Paneth Kolloquium Nördlingen, Abstract #0079, 2017.

[7] Lumpkin, G. R. and Zaikowski, A.: A method for performing magnetic mineral separations in a liquid medium, Am Min, 65, pp. 390–392, 1980.

[8] Bast, R., Scherer, E. E., Sprung, P., Fischer-Gödde, M., Stracke, A., and Mezger, K.: A rapid and efficient ion-exchange chromatography for Lu-Hf, Sm-Nd, and Rb-Sr geochronology and the routine isotope analysis of sub-ng amounts of Hf by MC.ICP-MS, JAAS, 30, pp. 2323-2333, 2015.

[9] Sprung, P., Kleine, T., and Scherer, E. E.: Isotopic evidence for chondritic Lu/H and Sm/Nd of the Moon, EPSL, 380, pp. 77-87, 2013.

[10] Sprung P., Scherer, E. E., Upadhyay, D., Leya, I., and Mezger, K.: Non-nucleosynthetic heterogeneity in non-radiogenic stable Hf isotopes: Implications for early solar system chronology, EPSL, 295, pp. 1-11, 2013.

EPSC Abstracts
Vol. 12, EPSC2018-372, 2018
European Planetary Science Congress 2018

Volatile outgassing and chemical speciation of the C-O-H system in the Earth´s Magma Ocean

Gianluigi Ortenzi (1,2), Frank Sohl (1) and Lena Noack (2)

(1) DLR German Aerospace Center, Institute of Planetary Research, Germany. (gianluigi.ortenzi@dlr.de). (2) Free University of Berlin, Germany.

Abstract

The aim of the research is to improve the present knowledge about the early phase of the Earth´s evolution, subsequent to the formation of the Moon. In this period the Earth was probably characterized by the presence of a magma ocean or several magma ponds and the silicate melt was the main source of volatiles for the early atmosphere. Specifically, the volcanic degassing and the volatile chemical speciation were investigated through the use of numerical modelling of the outgassed species. We analysed the volatile transition from the mantle to the atmosphere of the C-O-H system by the usage of the equilibrium constants and mass balance method. Considering the oxygen fugacity (fO_2) as one of the main factors that affects the chemical speciation, we observed changes in the ratio of reduced (H_2 and CO) or oxidized (H_2O and CO_2) species with different fO_2 values. The results show an interesting aspect of the interaction between the solid/melt phase and the gas phase since the volatile final composition is directly related to the melt oxygen fugacity.

Introduction

During the early phase of its evolution the Earth was likely characterized by a magma ocean stage [1]. The planet was completely or partly molten and there was a strong interaction between the silicate melt phase and the atmosphere. The aim of the research is to better characterize the volcanic degassing of the magma ocean and the related development of the early Earth's atmosphere. The volatile speciation and transition from the mantle to the atmosphere was analysed throughout numerical model simulations. In particular, the gas chemical speciation of the C-O-H system and its relationship with the redox state of the magma ocean are investigated.

Methods

The magma ocean outgassing and the volatile chemical speciation of the C-O-H system are investigated with the "Equilibrium and mass balance method" [2, 3]. The following reactions are simulated at different thermodynamic conditions and redox ambient.

$$H_2 + 1/2O_2 = H_2O \quad (1)$$

$$CO + 1/2O_2 = CO_2 \quad (2)$$

The equilibria (1, 2) are representative of the major volcanic volatile species of the C-O-H system. The composition of the gas phases are analysed with a fixed pressure of 1 bar and for a wide range of temperatures which are representative for the magma ocean context. The gas chemical speciation is influenced not only by the thermodynamic properties but, one of the most important aspects is the redox state of the melt during the outgassing process. The redox ambient of the magma ocean is represented by the level of oxygen fugacity of the melt silicate phase. In order to investigate the oxidation state of the melt, and therefore of the magma ocean, the oxygen fugacity is calculated using the well-known parametrizations for the most used petrological mineral buffers [4] and several meteoritic compositions [3]. To simulate the oxidizing ambient were selected the nickel-nickel oxide (NiNiO) and the quartz fayalite magnetite (QFM) buffers. In addition, to reproduce reducing conditions we selected the quartz-iron-fayalite (QIF) and iron wüstite (IW) buffers. Moreover, the calculated oxygen fugacity of undifferentiated chondritic meteorites (CI, CV, H and EH) and of differentiated eucrititc composition were considered in combination with the mineral buffers. This method connects the redox state of the melt to the outgassed volatile

species, since the calculated oxygen fugacity is employed in the numerical modelling of the gas phase equilibria.

Results

In the figure 1 we show the calculated oxygen fugacity using the parametrization from [3, 4].

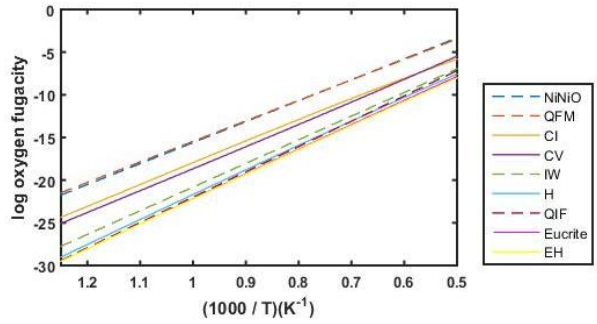

Figure 1. *Calculation of oxygen fugacity of some of the most used petrological mineral buffers and meteoritic compositions.*

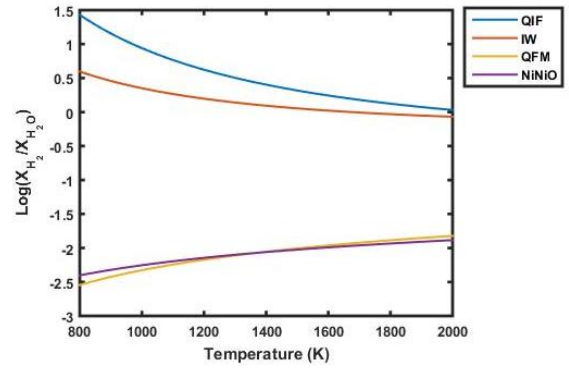

Figure 2. *The diagram shows the ratio of H_2/H_2O for different oxygen fugacity over temperature (P=1 bar).*

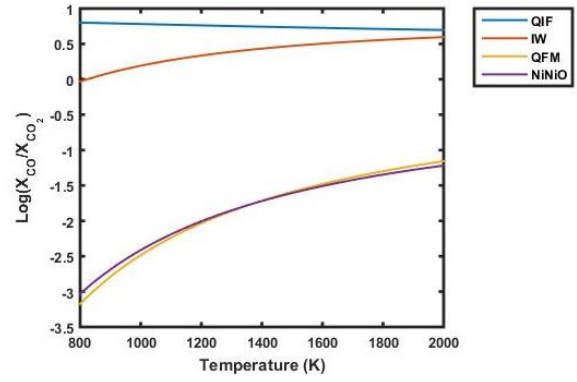

Figure 3. *CO/CO_2 ratio related to different redox conditions as function of temperature (P=1 bar).*

In the graphs we show the strong variations of oxygen fugacity for reducing or oxidizing ambient. The strong variation of oxygen fugacity deeply influences the gas chemical speciation. In figures 2 and 3 are plotted the ratio of H_2/H_2O and CO/CO_2 related to the redox conditions over an interval of temperatures and with a pressure of 1 bar. In the plots there is a strong change in the volatile composition connected to the redox state and to the temperature. For low temperatures and low oxygen fugacity (QIF and IW buffers) the main chemical species are CO and H_2. On the other hand in an oxidizing ambient (NiNiO and QFM buffers) the volatile composition is substantially H_2O and CO_2.

Discussion and conclusions

The main objective of our research was to shed light on the volatile outgassing during the Earth magma ocean stage and to the related composition of the early atmosphere. For this purpose, we simulated the volcanic outgassing and the speciation of the gas phases as a function of: pressure, temperature and redox state. As first step we calculated the oxygen fugacity for the most used petrological mineral buffers and for some meteoritic compositions. Subsequently, we estimated the outgassed volatile composition at different redox conditions. We observed that the redox state of the melt affects the gas phase composition. The main gas species under reducing conditions (QIF and IW mineral buffers) are H_2 and CO but for oxidizing conditions (NiNiO and QFM) H_2O and CO_2 are the dominant volatiles. In conclusion, this method permits to directly link the silicate melt to the outgassed species. The results show that the oxygen fugacity has a strong control on the volatile speciation and therefore, on the composition and evolution of the early Earth atmosphere.

Acknowledgements

This research has been funded by the Deutsche Forschungsgemeinschaft (SFB-TRR 170, subproject C5).

References

[1] Elkins-Tanton, 2008. Annu. Rev. Earth and Pl. Sci. 40:113-39.
[2] Gaillard and Scaillet, 2014. Earth and Pl. Sci. Let. 403:307–316.
[3] Schaefer and Fegley, 2017. Astrophy. J. 843:120 (18pp).
[4] Holloway et al., 1992. Eur. J. Min. 4, 105-114.

EPSC Abstracts
Vol. 12, EPSC2018-501, 2018
European Planetary Science Congress 2018

EPSC
European Planetary Science Congress

Realistic modeling of water transport to terrestrial planets by combining long-term dynamics and collision physics

Christoph Burger (1,2), Christoph Schäfer (2) and Akos Bazso (1)
(1) Department of Astrophysics, University of Vienna, Austria (c.burger@univie.ac.at), (2) Institut für Astronomie und Astrophysik, Eberhard Karls Universität Tübingen, Germany

Abstract

The last stage of terrestrial planet formation probably comprises the growth of planetary embryos – along with remaining smaller bodies – into the final planets, marked by chaotic interactions between the relatively few remaining large bodies, including similar-sized (giant) collisions and radial mixing of material that originated at very different locations in the disk. Despite the increasing trend of treating individual collisions beyond the (over-)simplified perfect merging assumption, this has not yet been applied consistently to (N-body) simulations of water transport to terrestrial planets, and none of the collision-outcome models that emerged in recent years seems to be well-suited for this task [1].

To close this gap between current planet formation models and the actual fate of volatile material in collisions, we present a framework to consistently combine the dynamics of late-stage planet formation with transfer and loss of material in collisions. Our results show that overall water losses in single collisions can often be tens of percent, and in the common hit-and-run encounters the smaller body is frequently stripped of the majority of its pre-collision volatiles. This strongly suggests the necessity to track both large survivors of a hit-and-run collision (and their retained and transferred volatiles) through the further N-body evolution.

1. Methods

We use a hybrid approach to combine the dynamical long-term evolution, with fully three-dimensional hydrodynamical simulations of individual collisions. For modeling the N-body dynamics over 10s to 100s of Myrs we use the REBOUND[1] package [3], while collisions are simulated with our SPH code [4]. The latter allows for optional solid-body rheology including a damage model, multiple materials, along with self-gravity, and is implemented to utilize powerful GPU hardware to allow large particle numbers combined with still practical computing times.

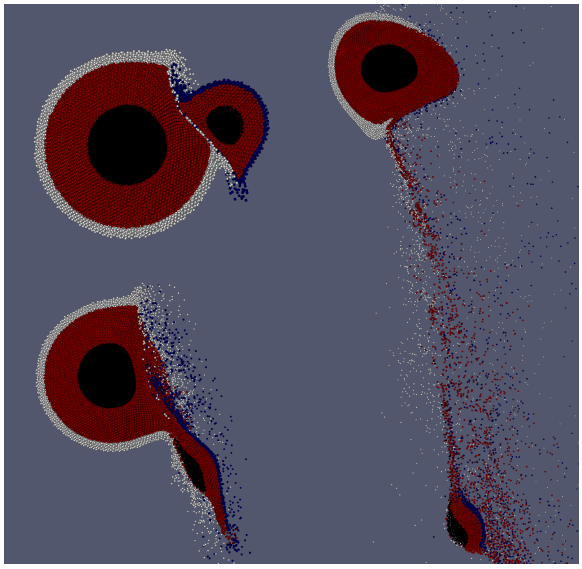

Figure 1: SPH collision snapshots (cut views), illustrating water transfer and loss in a typical hit-and-run encounter. The color-coding shows the bodies' composition, where the initial water inventories of projectile and target are highlighted in different colors (blue and white). The total colliding mass is 10^{23} kg, $\gamma =$ 1:9, $v/v_{\rm esc} = 2.5$, and $\alpha = 45°$.

2. Results and conclusions

Collisions between similar-sized bodies exhibit a diverse range of possible outcomes between (partial) accretion, hit-and-run, and (partial) erosion. In previous work [2] we already showed that not only the impact velocity ($v/v_{\rm esc}$), impact angle (α) and projectile-to-target mass ratio (γ), but also the total colliding mass

[1]REBOUND can be downloaded freely at http://github.com/hannorein/rebound.

are important for determining volatile losses. Fig. 2 summarizes the total amount of water loss (combined for all large fragments) for a suite of collision scenarios. Highly energetic encounters result in losses well above 50%, but already moderate collision parameters can lead to values in the tens-of-% range.

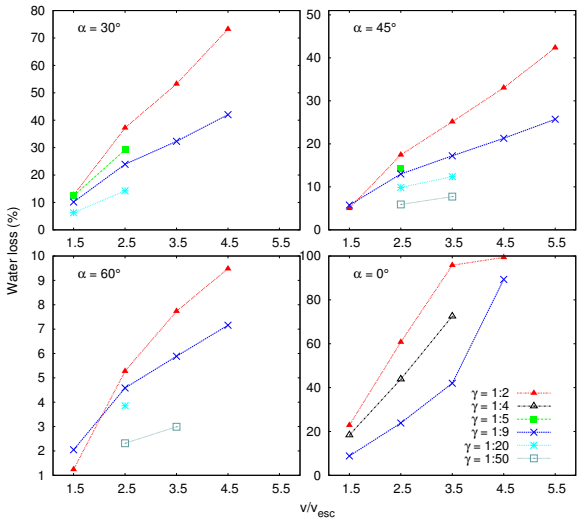

Figure 2: Overall water losses of projectile+target as a function of $v/v_{\rm esc}$, for a large variety of impact angles α and mass-ratios γ, from [1]. The strong dependency on each of these parameters is clearly visible.

Especially for relatively fast and non-central encounters, so-called hit-and-run, the individual post-collision water inventories become important, and great differences between the 2 large fragments can emerge, as illustrated in Fig. 3. While the most-massive body remains rather unaltered, it is often especially the smaller one of the colliding pair that is affected down to the core, and efficiently stripped of volatiles, as exemplified in Fig. 1. Therefore combining physically correct collision outcomes with N-body dynamics has to include the 2 large hit-and-run survivors separately, even if this results in a considerable computational slow-down since the number of bodies decreases naturally much slower with time (compared to having strictly only 1 survivor).

Acknowledgements

C. B. and A. B. acknowledge support by the FWF Austrian Science Fund projects S11603-N16 and S11608-N16, and C. S. by the German Research Foundation (DFG) through grant no. INST 37/935-1 FUGG.

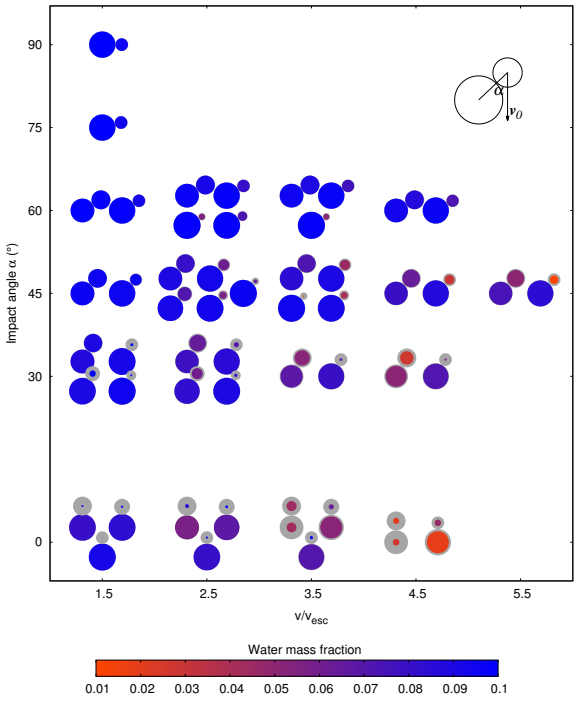

Figure 3: Results of similar-sized, giant collisions, including the distinction between the largest and 2nd-largest fragment, in a grid of $v/v_{\rm esc}$ and α, and for different γ (sizes of the light-grey pictograms) from [1]. All circle-sizes are $\propto$ mass$^{1/3}$, and the colored circles indicate post-collision mass. The pre-collision water-mass fractions are always 0.1 for both bodies.

References

[1] C. Burger, T. I. Maindl, and C. M. Schäfer. Transfer, loss and physical processing of water in hit-and-run collisions of planetary embryos. *Celestial Mechanics and Dynamical Astronomy*, 130:2, January 2018.

[2] C. Burger and C. M. Schäfer. Applicability and limits of simple hydrodynamic scaling for collisions of water-rich bodies in different mass regimes. *Proceedings of the First Greek-Austrian Workshop on Extrasolar Planetary Systems*, pages 63–81, March 2017.

[3] H. Rein and S.-F. Liu. REBOUND: an open-source multi-purpose N-body code for collisional dynamics. A&A, 537:A128, January 2012.

[4] C. Schäfer, S. Riecker, T. I. Maindl, R. Speith, S. Scherrer, and W. Kley. A smooth particle hydrodynamics code to model collisions between solid, self-gravitating objects. A&A, 590:A19, April 2016.

EPSC Abstracts
Vol. 12, EPSC2018-566, 2018
European Planetary Science Congress 2018

The effect of temperature distribution in the lunar mantle on the bulk composition of the Moon

Ekaterina Kronrod, Oleg Kuskov and Victor Kronrod

Vernadsky Institute of Geochemistry and Analytical Chemistry (GEOKHI RAS), Moscow, Russia (e.kronrod@gmail.com)

Abstract

The purpose of the present study is to evaluate the lunar bulk composition (BSM) and the composition of the three-layer mantle based on a joint inversion of lunar mass and moment of inertia, and the mantle seismic velocity profiles in combination with Gibbs free energy minimization. We obtained that regardless of the thermal state, BSM possess almost constant values of bulk FeO ~ 12-13 wt.% and MG# 80-81.5, which id significantly different from those of the bulk-silicate Earth (BSE). The FeO content and MG# are approximately identical in the upper and lower mantle. The abundance of SiO_2 slightly depends on the thermal state. On the contrary, there are two different groups for the lunar abundance of alumina depending on the thermal state: 1) Cold models of BSM (3-4.6 wt.% Al_2O_3) are comparable to the Al_2O_3 content for the BSE; 2) Hot models (bulk Al_2O_3 is 1.2 – 1.7 × BSE). The simulation results suggest that the lunar mantle is stratified by chemical composition.

1. Introduction

The chemical composition of the Moon should be considered as a fundamental geochemical constraint when testing cosmogonic models of its origin. One of the most important problems of lunar geochemistry is the determination of its bulk composition - mainly the concentrations of rock-forming oxides SiO_2, Al_2O_3, CaO, FeO and the MG# affecting mineralogy and physical properties (density (ρ), bulk (K_S) and shear (G) moduli, V_P and V_S) of the mantle. The purpose of this work is to evaluate these geochemical parameters and to construct a model of chemical composition of the Moon based on a joint inversion of lunar mass and moment of inertia, the mantle P-, S-velocity profiles and petrological models methods.

2. Data and method

We investigate the thermal state and chemical composition of the silicate portion of the Moon (crust + mantle; BSM) for the magma ocean model (wich implies that modern composition of uniformly mixed overlying shells is identical with the bulk composition of the magma ocean, and reflect the bulk composition of the silicate Moon). We consider a five-layer model of the internal structure of the Moon including the crust, three zones of the mantle (the upper (39-240 km), the middle (240-750 km) and the lower mantle (750 km - core)) and Fe-S core. The input parameters of the model are the lunar mass and moment of inertia [1], the composition, the mean density and thickness of the crust, the seismic P- and S-wave velocities in the mantle [2,3], the oxide concentration interval in the NaTiCFMAS system, the average density of the Fe-S core.

The modeling of the composition and physical properties of the Moon was performed in the NaTiCFMAS system using Monte Carlo method and Gibbs free energy minimization combined with a Mie-Grüneisen equation of state of minerals described in detail in our previous publications [4,5]. The following ranges of oxide concentrations in the mantle (wt.%) were considered: $25 \le MgO \le 45\%$, $40 \le SiO_2 \le 55\%$, $5 \le FeO \le 15\%$, $0.1 \le CaO$, $Al_2O_3 \le 7\%$, where the concentrations of Al_2O_3 and CaO are related by the dependence of $CaO/Al_2O_3 \sim 0.8$.

3. Results

Since the temperature at different depths is not exactly known [5,6], the mean volume mantle temperature T_{mean}, controlling the mantle mineral composition and physical properties, is chosen as an integral characteristic of the thermal state of the Moon, which for our model is calculated from the

expression: $T_{mean} = (T_uV_u + T_mV_m + T_lV_l)/(V_u + V_m + V_l)$, where T_u, T_m, T_l are the mean temperatures (°C) in the three zones of the mantle, V_u, V_m, V_l are the volumes of the upper, middle and lower mantle. In terms of T_{mean}, all thermal models can be divided into "cold" ones with T_{mean} ~ 690-860°C and "hot" ones with T_{mean} ~ 925-1075°C (fig. 1).

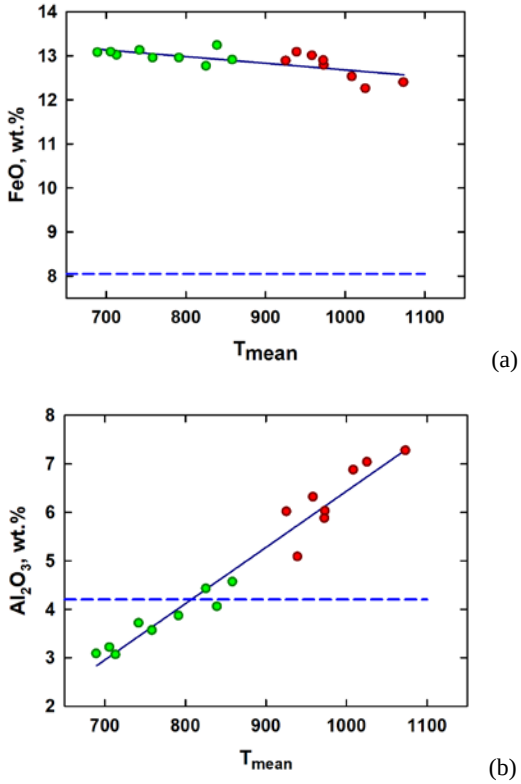

Figure 1: The contents of FeO, Al_2O_3, SiO_2 and MG# in the silicate portion of the Moon (mantle + crust) calculated from geodetic and seismic data as a function of mantle temperature (T_{mean}). Dots - the mean values of FeO (a) and Al_2O_3 (b) concentrations under the assumption of a normal distribution. Red color – "hot" models, green color – "cold" models. Dashed line - the parameters for BSE (Ringwood, 1977; McDonough, 1990, Dauphas et al., 2014).

3. Conclusions

Regardless of the thermal state, BSM is characterized by almost constant bulk FeO ~ 12-13 wt.% and MG# 80-81.5, which significantly differs from those for the bulk-silicate Earth (BSE). The FeO content of 11-14 wt.% and MG# 80-83 are approximately identical in the upper and lower mantle. The abundance of SiO_2 slightly depends on the thermal state and is 50-55% in the upper mantle and 45-50% in the lower mantle. On the contrary, there are two different groups for the lunar abundance of alumina depending on the thermal state: 1) Cold models of BSM (3-4.6 wt.% Al_2O_3) are comparable to the Al_2O_3 content for the BSE; 2) Hot models bulk Al_2O_3 is 1.2 – 1.7 × BSE. The results indicate a gradual increase in the alumina content from the upper mantle (1-2%) to the lower one up to 4-7 wt.% Al_2O_3 with a garnet amount up to ~20 wt.%. The simulation results suggest that the lunar mantle is stratified by chemical composition. However, the question of the similarity and / or difference in their composition with regard to the abundance of refractory elements remains unresolved and requires further research.

Acknowledgements

This work was supported in part by the Russian Foundation for Basic Research (RFBR) under Grant 18-05-00225 and Program 17 of the Presidium of the Russian Academy of Sciences

References

[1] Williams, J, Konopliv A., Boggs D., Park R., Yuan D.-N., Lemoine F, Goossens S., and Zuber M. T.: Lunar interior properties from the GRAIL mission, J. Geophys. Res., Vol. 119. doi: 10.1002/2013JE004559, 2014.

[2] Lognonn´e, P.: Planetary seismology. Ann. Rev Earth Planet. Sci. Vol. 33, pp. 571–604, 2005.

[3] Gagnepain-Beyneix, J., Lognonné P., Chenet H., Lombardi D. and Spohn T.: A seismic model of the lunar mantle and constraints on temperature and mineralogy, Phys. Earth and Planet Int., Vol. 159, pp. 140-166, 2006.

[4] Kuskov O. and Kronrod V.: Geochemical constraints on the model of the composition and thermal conditions of the Moon according to seismic data, Izv. Phys. Solid Earth, Vol. 45, pp. 753–768, 2009.

[5] Kuskov O., Kronrod, V. and Kronrod, E.: Thermo-chemical constraints on the interior structure and composition of the lunar mantle Phys. Earth Planet. Inter., Vol. 235, pp. 84-95, 2014.

[6] Khan, A., Connolly, J., Pommier, A. and Noir, J.: Geophysical evidence for melt in the deep lunar interior and implications for lunar evolution. J. Geophys. Res. Planets. Vol.119, pp. 2197–2221, 2014.

EPSC Abstracts
Vol. 12, EPSC2018-688, 2018
European Planetary Science Congress 2018

A long-lived lunar magma ocean

Maxime Maurice (1), Nicola Tosi (1,2), Sabrina Schwinger (1) and Doris Breuer (1)
(1) German Aerospace Center (DLR), Berlin, Germany, (2) Technische Universität Berlin, Germany
(maxime.maurice@dlr.de)

1. Introduction

The moon is thought to originate from a collision between the early Earth and a Mars-sized impactor. Such a giant impact would have left a large quantity of the lunar mantle molten, resulting in a global magma ocean. A large part (about 80%) of the lunar magma ocean (LMO) solidifies in around 1000 years by efficient radiative heat loss at its molten surface, until a solid crust forms by flotation of plagioclase. The heat is then lost by conduction through the growing crust, which is a much less efficient regime, delaying the complete solidification of the LMO to a few tens of millions of years. However, the lunar anorthositic crust formed over a time span of ~200 Myr [1], still longer than what LMO solidification models suggest. Based on the observation that the LMO solidification time scale is compatible with solid cumulates overturn, we show that secondary melting generated by hot plumes after onset of solid-state convection below the solidifying LMO represents an important heat source for the LMO by extracting hot melt from the cumulates into the LMO, that can suffice to delay the complete solidification by about 200 Myr.

Furthermore, the onset of solid-state convection in the solidifying cumulates help entrain the late crystallized Ilmenite bearing cumulates (IBC) into the mantle before a stiff stagnant lid forms and traps the IBC. This constitutes an alternative sinking mechanism to the usually assumed post-solidification overturn.

2. Model

We use the model described in [2] to perform 2D and 3D simulations of solid-state convection on the cumulates below a self-consistently solidifying LMO. The initial structure of the mantle is computed from fractional crystallization of a global LMO using alphaMELTS, and the solidification of the LMO and the growth of the flotation crust are parametrized by solving the energy conservation equilibrating the outgoing heat flux through the crust with the incoming conductive and “heat piping” heat fluxes as well as the internal heating of the LMO from radioactive decay. Figure 1 represents how the different systems (core, solid cumulates, LMO and crust) are thermally coupled.

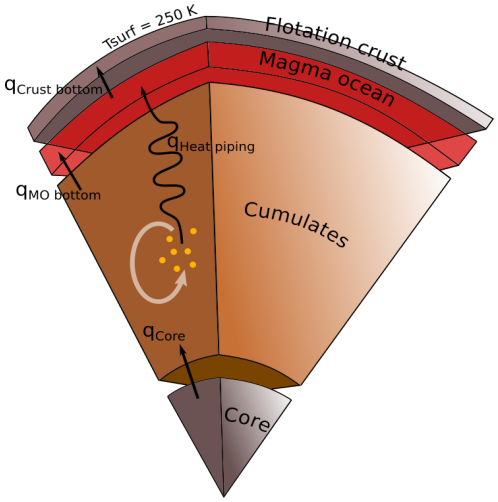

Figure 1: Thermal couplings between the different layers of the system. The thermal energy is conserved for each of the four systems, the interfacial heat fluxes (black arrows) and the surface temperature providing the boundary conditions. The heat piping flux originates from the melting induced by solid-state convection in the cumulates (white arrow). Internal heating by radioactive decay is also included.

3. Results

We investigate the influence of heat piping on the LMO's crystallization duration and the entrainment of IBC in the lunar mantle.

3.1. LMO duration

We varied the reference viscosity of the lunar mantle as a parameter, causing different overturn time scales and convective intensities, resulting in different heat piping efficiency. While, for a high reference viscosity

(~10^{22} Pa s) no overturn occurs during LMO solidification and the heat piping flux is zero, lower (but still realistic) values of the reference viscosity (~10^{19} Pa s) result in rapid onset of solid-state convection generating an intense heat piping flux due to decompression melting in the cumulates. This supplementary heat source significantly prolongs the LMO duration, up to ~200 Myr, matching the isotopic age measurements of the lunar crust.

3.2. IBC entrainment

Entrainment of the late crystallized IBC is needed to produce the Moon's surface high-Ti mare basalts and picritic glasses by secondary melting [3]. However, the IBC crystallize at low temperature and remain trapped in the stagnant lid in models where solid-state convection starts after the whole lunar mantle is solid [3]. We showed in a previous work [2] that onset of solid-state convection during the magma ocean solidification provides an efficient means to mix composition heterogeneities inherited from fractional crystallization. We show that when cumulates overturn occurs during LMO solidification, a substantial part of the IBC is entrained in the bulk convecting mantle, and Ilmenite is present in re-melting plumes even long after the end of the LMO solidification.

References

[1] Elkins-Tanton L. *et al*., EPSL, Vol. 304, pp. 326-336, 2011.

[2] Maurice M. *et al*., JGR: Planets, Vol. 122, pp. 577-598, 2017.

[3] Elkins-Tanton L, EPSL, Vol. 196, pp. 239-249, 2002.

EPSC Abstracts
Vol. 12, EPSC2018-1000, 2018
European Planetary Science Congress 2018

Forming a Lunar Dichotomy by Giant Impact Melting

Sabrina Schwinger (1) and MengHua Zhu (2)
(1) German Aerospace Center (DLR), Berlin, Germany (sabrina.schwinger@dlr.de)
(2) Space Science Institute, Macau University of Science and Technology, Macau (mhzhu@must.edu.mo)

Abstract

An impact on the lunar nearside can potentially explain several aspects of the lunar dichotomy, including differences in crustal thickness, the lateral extent of the lunar lowlands and a high concentration of thorium and other incompatible elements (KREEP) in the Procellarum KREEP Terrane (PKT) on the lunar nearside. We employ a multi-step modeling approach to simulate the compositional evolution of the lunar interior and explore, which aspects of the lunar dichotomy can be explained by a giant impact on the lunar nearside.

1. Introduction

The Moon is characterized by a global asymmetry comprising distinct differences in crust thickness, crater density, surface compositions and heat flow between the lunar nearside and farside [1, 2, 3]. The lunar farside is covered by an old, heavily cratered anorthositic crust, while the lunar nearside is dominated by mare basalts. Recent GRAIL data [4] indicate a dichotomy in crustal thickness with up to 60 km on the lunar farside and about 25km in the Procellarum region on the lunar nearside. Heat flow measurements indicate an increased heat flow in the Procellarum region [5] that coincides with high amounts of Fe, Ti, Th and KREEP [2]. Multiple models have been proposed to explain different aspects of the lunar dichotomy, including asymmetric crystallization of the lunar crust [6] and asymmetries in mantle convection [7]. In this study we explore, which aspects of the lunar dichotomy can be explained by a giant impact and subsequent partial melting of the mantle on the lunar nearside.

2. Model

1.1 Impact

We use iSALE [8] to model the impact of a projectile with a diameter of 780 km on he nearside of the Moon with an impact velocity of 6.4 kms^{-1}. The projectile was assumed to be differentiated into a FeS core and a silicate mantle from a bulk H chondritic composition. The lunar mantle and crust constituting the target were assumed to have formed by fractional crystallization of a global lunar magma ocean (LMO) with main oxide contents as proposed by [9]. We modeled LMO crystallization with alphaMELTS [10, 11,12], assuming that all crystallizing plagioclase floats to the surface to form an anorthositic crust and the remaining mantle cumulate was mixed by solid state convection. It has been shown that dense, Ti-rich, ilmenite bearing cumulates (IBC) can be partially entrained in the deeper mantle, resulting in elevated IBC concentrations both at the core mantle boundary and at the base of the crust [13]. We used this distribution of IBC in the mantle after convective overturn to calculate the composition of the lunar mantle. The mantle temperature was assumed to be at the solidus at the time of the giant impact.

1.1 Partial melting

For each material considered in the impact model we assumed specific solidus and liquidus functions and determined the compositions of partial melts at different degrees of melting using alphaMELTS [10, 11,12] and experimental data for FeS and anorthosite compositions. Using this information, we calculated the degree of melting and the respective composition of the partial melts in different regions of the lunar mantle depending on the local post impact temperature. We assumed that above a minimum degree of melting of 3% the partial melts could migrate to the surface and form a melt pool. The composition and volume of this melt pool was calculated by mixing the compositions of all partial melts. In order to determine the thickness of the secondary plagioclase floatation crust formed by melt pool solidification and the composition of the newly formed upper mantle, we modeled the fractional crystallization of the melt pool using alphaMELTS [10, 11,12].

3. Results and Discussion

Assuming that the partial melts rise radially to the surface and form a melt pool of homogeneous thickness, the melt pool has a radius of ~1600km and a depth of ~80km. The dimension of the melt pool is consistent with size of the mare basalt region [14]. The thickness of the secondary crust crystallizing from the melt pool is in the order of 20 km, which is consistent with the average crust thickness of about 25 km in the Procellarum region inferred from GRAIL data [4]. The post impact melting process leads to a local enrichment of heat producing radioactive isotopes of Th, U and K. Compared to the upper mantle at the lunar farside, the Th concentrations at the impact site are elevated by a factor of about 2.5 in the upper 80km of the mantle. This local Th enrichment is about 6 times lower than the one assumed by [15] to explain the different durations of volcanic activity on the lunar nearside and farside. The Th content of the melt pool strongly depends on the composition of the mantle at the time of the impact, which in turn depends on the current distribution of KREEP bearing IBC material in the lunar mantle. Thus a different timing of the impact with respect to the onset of IBC crystallization and entrainment might lead to differences in the melt pool composition and thus the distribution of radiogenic heat sources.

4. Conclusions

A large impact on the Procellarum region at the lunar nearside can reproduce several aspects of the lunar dichotomy including the extent and crustal thickness of the nearside lowlands and the presence of a local enrichment of the uppermost mantle below the impact site. However, the modeled degree of enrichment is probably too low to explain the different durations of volcanic activity on the lunar nearside and farside. Thus, further refinement of the model is required to obtain results that are quantitatively consistent with the distribution and formation ages of mare basalts.

Acknowledgements

We gratefully acknowledge the developers of iSALE, including Gareth Collins, Kai Wünnemann, Dirk Elbeshausen, Boris Ivanov and Jay Melosh. This work was funded by the Deutsche Forschungsgemeinschaft (SFB-TRR 170, C4).

References

[1] Zuber, M. T., Smith, D. E., Lemoine, F. G. & Neumann, G. A.: The shape and internal structure of the moon from the Clementine mission. Science 266, 1839–1843, 1994. [2] Lawrence, D. J. Global elemental maps of the moon: the Lunar Prospector gamma-ray spectrometer. Science 281, 1484–1489, 1998. [3] Jolliff, B. L., Gillis, J. J., Haskin, L. A., Korotev, R. L. & Wieczorek, M. A.: Major lunar crustal terranes: surface expressions and crust-mantle origins. J. Geophys. Res. 105, 4197–4216, 2000. [4] Wieczorek MA, Neumann GA, Nimmo F, Kiefer WS, Taylor GJ, Melosh HJ, Phillips RJ, Solomon SC, Andrews-Hanna JC, Asmar SW, Konopliv AS.: The crust of the Moon as seen by GRAIL. Science, 1231530, 2012. [5] Warren, P.H. and Rasmussen, K.L.: Megaregolith insulation, internal temperatures, and bulk uranium content of the Moon. Journal of Geophysical Research: Solid Earth, 92(B5), pp.3453-3465, 1987. [6] Wasson, J. T. and Warren, P. H.: Contribution of the mantle to the lunar asymmetry. Icarus 44, 752–771, 1980. [7] Loper, D. E. and Werner, C. L.: On lunar asymmetries 1. Tilted convection and crustal asymmetry. J. Geophys. Res. Planets 107, 131–137, 2002. [8] Wünnemann, K., Collins, G.S. and Melosh, H.J.: A strain-based porosity model for use in hydrocode simulations of impacts and implications for transient crater growth in porous targets. Icarus, 180(2), pp.514-527, 2006. [9] O'Neill, H.S.C.: The origin of the Moon and the early history of the Earth - a chemical model. Part 1. The Moon. Geochem. Cosmochim. Acta 55, 1135–1157, 1991. [10] Smith PM, Asimow PD: Adiabat_1ph: a new public front-end to the MELTS, pMELTS, and pHMELTS models. Geochem Geophys Geosys 6:2004GC000816, 2005. [11] Ghiorso MS, Sack RO: Chemical mass transfer in magmatic processes IV. A revised and internally consistent thermodynamic model for the interpolation and extrapolation of liquid–solid equilibria in magmatic systems at elevated temperatures and pressures. Contrib Mineral Petrol 119:197–212, 1995. [12] Ghiorso MS, Hirschmann MM, Reiners PW, Kress VC: The pMELTS: a revision of MELTS for improved calculation of phase relations and major element partitioning related to partial melting of the mantle to 3 GPa. Geochem Geophys Geosyst 3:2001GC000217, 2002. [13] Yu et al. (2018), in prep. [14] Jolliff BL, Gillis JJ, Haskin LA, Korotev RL, Wieczorek MA.: Major lunar crustal terranes: Surface expressions and crust-mantle origins. Journal of Geophysical Research: Planets. 105(E2):4197-216., 2000. [15] Laneuville, M., Taylor, J. and Wieczorek, M.: Lunar Radioactive Heat Source Distribution and Magnetic Field Generation. 49th Lunar and Planetary Science Conference, 2018.

EPSC Abstracts
Vol. 12, EPSC2018-1097, 2018
European Planetary Science Congress 2018

A SINGLE PLUME UPWELLING ON LUNAR NEAR SIDE THAT PROVIDES A SOURCE FOR TITANIUM-RICH VOLCANISM.

Y. Zhao[1], Ana-Catalina Plesa[2], Doris Breuer[2], Matthieu Laneuville[3], Wim van Westrenen[1], [1]Faculty of Science, Vrije Universiteit Amsterdam, the Netherlands, [2]Department of Planetary Physics, German Aerospace Center (DLR), Berlin, Germany, [3]Earth-Life Science Institute (ELSI), Tokyo Institute of Technology, Tokyo, Japan, email y.zhao@vu.nl

Introduction: The most striking feature of the lunar surface is the dichotomy between the near side and the far side. The mare basalts that cover about a third of the near-side surface are present on only 1% of the far side. The Lunar Prospector mission discovered that the distribution of thorium on the lunar surface is concentrated in the Procellarum KREEP terrain (PKT), whose location strongly correlates to that of a nearside mare basalt region [1], and to a lesser extent in the far-side South Pole–Aitken basin. The lack of KREEP signatures in the material ejected from many large far-side impact basins implies that the source of KREEP is concentrated in the near-side hemisphere [2].

The asymmetrical distribution of mare basalts and KREEP on the lunar surface has been proposed to be due to a single-plume upwelling toward the near side. Zhong et al. [3] argued that this upwelling stems from dense ilmenite-bearing cumulates (IBC) that sank to the core-mantle boundary from under the crust where IBC crystallized in the late stages of lunar magma ocean solidification. The IBC contains high concentrations of heat-producing elements, making it thermally buoyant enough to rise after the initial sinking. Parmentier et al. [4] studied the Rayleigh-Taylor instability developed in a dense layer lying on top of another layer, simulating the gravitationally unstable IBC after the solidification of the lunar magma ocean. They suggested that spherical harmonic degree 1 is the fastest growing instability when the top layer is sufficiently thick, and when the viscosity of the top layer is ~4 orders of magnitude lower than the underlying mantle.

This study aims to investigate the possibility of localizing key ingredients for lunar volcanic activities, including sources for titanium and radioactive elements, to the near side of the Moon after solidification of the magma ocean, using numerical models that simulate both the downwelling of IBC and the upwelling that give rise to volcanism. In particular, we describe our preliminary results using asymmetrical crustal thickness and distribution of KREEP as an initial condition.

Numerical method: Our numerical models are performed in a 2-D cylindrical domain. The lunar mantle is simulated using the Boussinesq approximation as a fluid with infinite Prandlt number. Finite volume code Gaia [5] is used to solve the conservation equations of mass, momentum, and energy. The advection of chemical components is implemented using the particle-in-cell method [6]. The mantle domain is heated from within by radioactive decay and from below by a cooling core. A reference viscosity of $1x10^{20}$ Pa s is used, resulting in a thermal Rayleigh number of $1x10^{7}$. We use a fine mesh with a radial resolution of 1.7 km throughout the domain. More than 90 million tracers are used to track various material properties, including density, viscosity and concentrations of heat-producing elements.

Our models start when the lunar magma ocean has solidified. The stratified cumulates are characterized by varying density, viscosity, and distribution of heat-producing elements [7]. Viscosity is computed by using a temperature- and pressure-dependent Arrhenius law for diffusion creep. In addition to that, IBC have their viscosities one order of magnitude lower than calculated from the Arrhenius model, taking into account the low viscosity of ilmenite [8]. For density and concentration of heat-producing elements, we use a weighted arithmetic average according to their concentration when different chemical components are mixed. Viscosity is combined to a product of the viscosity of all compositions to the power of their relative concentration.

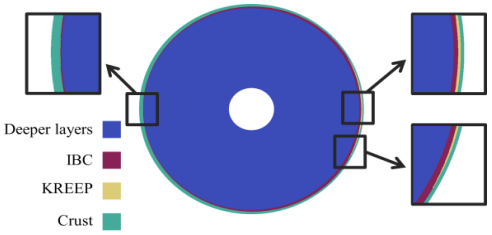

Figure 1. The asymmetrical distribution of crustal thickness, IBC, and KREEP in the initial condition.

The crust has a thermal conductivity of 1 W/m/K, taking into account the low thermal conductivity of plagioclase, and the porous top layers of the crust. The initial crustal thickness is a minimum of 20 km on the near side and a maximum of 40 km on the far side, and we use a sine function to model its variation. KREEP, having the same density and viscosity as IBC while containing higher concentrations of heat-producing elements, is localized in a cylindrical cap of 40 degrees, which mimics the PKT region subsurface. Its thickness is 20 km where crustal thickness is 20 km, and gradually decreases to 0 towards the PKT edge. Figure 1 shows these initial conditions.

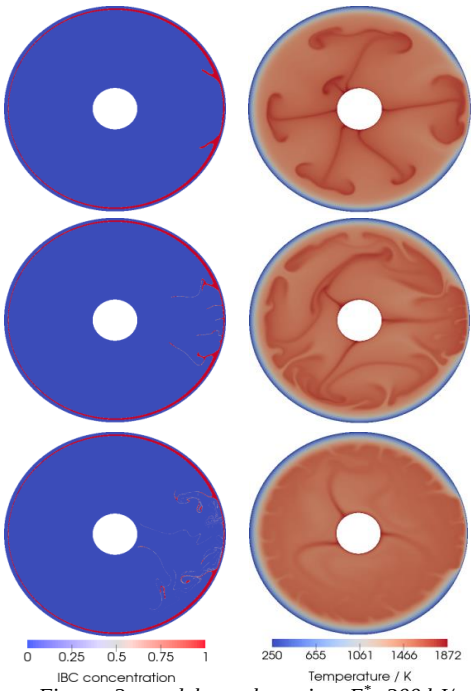

Figure 2. model results using E^*=300 kJ/mol. Here IBC concentration includes both the IBC and KREEP in Figure 1.

Results: Two sets of model results are shown in Figures 2 and 3, corresponding to activation energies E^* of 300 kJ/mol and 100 kJ/mol, respectively, in the Arrhenius viscosity model. Both models show the sinking of dense IBC in two diapirs that correspond to the edges of the PKT region. An upwelling remains under the PKT region, due to the region's high heat production, though the convective pattern evolves differently in the two models. We can see from Figure 2 that when E^*=300 kJ/mol, the onset of convection is driven by several upwellings at the core-mantle boundary (CMB). When E^*=100 kJ/mol, as shown in Figure 3, the onset of convection is driven by sinking IBC. During the sinking of IBC along the edges of PKT, an upwelling is formed underneath the PKT. Foundered IBC at the CMB are then brought up by the near-side upwelling, providing a source of titanium and heat-producing elements to the near side.

Discussion and conclusion: Our preliminary results show that the behavior of IBC overturn under an asymmetrical initial condition is sensitive to the temperature dependence of viscosity. When E^*=100 kJ/mol, foundered IBC is brought to the surface through a near-side single-plume upwelling. This mechanism may explain titanium-rich sources for nearside volcanism. Our continued numerical experiments will further test the effects of a range of other parameters, including the reference viscosity, which may also play an important role in the convective pattern.

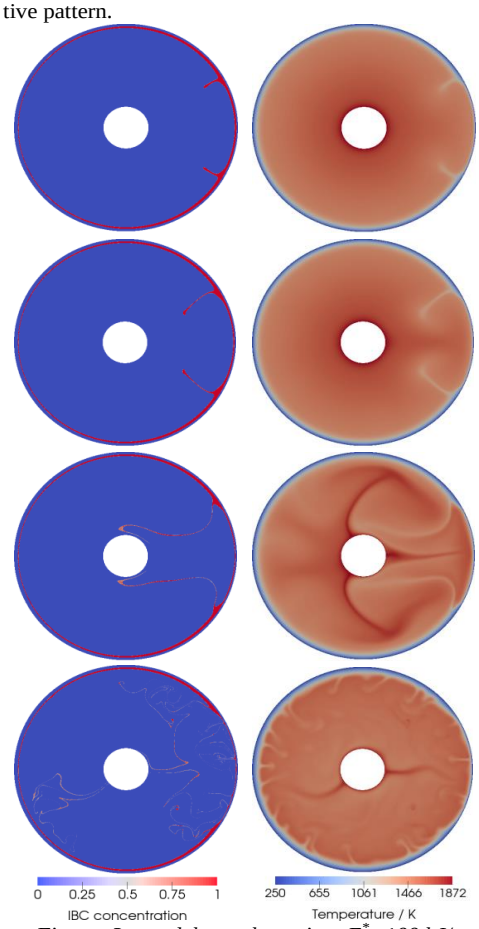

Figure 3. model results using E^*=100 kJ/mol. Here IBC concentration includes both the IBC and KREEP in Figure 1.

Acknowledgement: This work was carried out on the Dutch national e-infrastructure with the support of SURF Cooperative, and also the Cray XC30 system of the Earth-Life Science Institute in Tokyo.

References: [1] Jolliff B. L. et al. (2000) *JGR*, 105, 4197–4216 [2] Warren P. H. (2001) *GRL.*, 28, 2565–2568 [3] Zhong S. et al. (2000) *EPSL*, 177, 131–140 [4] Parmentier E. M. et al. (2002) *EPSL*, 201, 473–480 [5] Plesa A-C. et al., (2012) In: Rueckemann, C.-P. (Ed.), *IGI Global*, 302–323 [6] Hüttig C. et al. (2013) *PEPI*, 220, 11–18 [7] de Vries J. (2012) Chapter 5, *PhD diss*, Utrecht University. [9] Dygert N., et al. (2016) *GRL*, 43, 532-540